



CHORUS

This is the accepted manuscript made available via CHORUS. The article has been published as:

## Evidence for Interlayer Coupling and Moiré Periodic Potentials in Twisted Bilayer Graphene

Taisuke Ohta, Jeremy T. Robinson, Peter J. Feibelman, Aaron Bostwick, Eli Rotenberg, and Thomas E. Beechem

Phys. Rev. Lett. **109**, 186807 — Published 2 November 2012

DOI: [10.1103/PhysRevLett.109.186807](https://doi.org/10.1103/PhysRevLett.109.186807)

## Evidence for interlayer coupling and moiré periodic potentials in twisted bilayer graphene

Taisuke Ohta,<sup>1</sup> Jeremy T. Robinson,<sup>2</sup> Peter J. Feibelman,<sup>1</sup> Aaron Bostwick,<sup>3</sup> Eli Rotenberg,<sup>3</sup> Thomas E. Beechem<sup>1</sup>

<sup>1</sup> Sandia National Laboratories, Albuquerque, New Mexico 87185

<sup>2</sup> Naval Research Laboratory, Washington, D.C. 20375

<sup>3</sup> Advanced Light Source, Lawrence Berkeley National Laboratory, Berkeley, California 94720

We report a study of the valence band dispersion of twisted bilayer graphene using angle-resolved photoemission spectroscopy and *ab initio* calculations. We observe two non-interacting cones near the Dirac crossing energy, and the emergence of van Hove singularities where the cones overlap for large twist angles ( $>5^\circ$ ). Besides the expected interaction between the Dirac cones, mini-gaps appeared at the Brillouin zone boundaries of the moiré superlattice formed by the misorientation of the two graphene layers. We attribute the emergence of these mini-gaps to a periodic potential induced by the moiré. These anti-crossing features point to coupling between the two graphene sheets, mediated by moiré periodic potentials.

Much effort has been directed toward using graphene in electronics and optoelectronics to exploit its high electrical conductivity and unique Dirac fermion quasi-particles.<sup>1</sup> With continuing progress in fabricating large-area graphene sheets,<sup>2,3</sup> one can now transfer one or a few graphene layers onto desired substrates<sup>4</sup> or construct hybrid multilayer structures.<sup>5,6</sup> Such transfer processes unavoidably introduce azimuthal misorientation, or twist. Many growth processes also result in twisted multilayers.<sup>7,8,9</sup> Envisioning applications involving more than one graphene sheet for specific properties<sup>10,11,12</sup> therefore makes it important to understand the electronic properties of “twisted graphene.”<sup>13</sup>

A key issue is the electronic interaction between twisted graphene layers. Theoretical approaches have shown that for twisted bilayer graphene (TBG), interlayer interaction occurs at discrete locations within the Brillouin zone (BZ).<sup>14,15,16,17,18</sup> Depending on twist angle, one can expect Fermi velocity reductions or emergence of van Hove singularities (vHs). Transport measurements imply that TBG’s charge carriers near the Dirac crossing energy ( $E_D$ ) behave as if in an isolated graphene sheet, confirming theoretical predictions for a large twist angle.<sup>19,20</sup> Scanning tunneling microscopy (STM) and Raman spectroscopy support the notion of interlayer interaction through the presence of vHs<sup>21,22,23</sup> and a moiré.<sup>24</sup> On the contrary, angle-resolved photoemission spectroscopy (ARPES) investigations of a similar system, twisted *multilayer* graphene (i.e.,  $>$ two layers, typically grown on the carbon-face of silicon-carbide (SiC)), provided no evidence of interlayer interaction across the entire BZ,<sup>25,26,27</sup> despite formation of moiré.<sup>28</sup> So far, ARPES has provided little information regarding the TBG’s interlayer interaction.<sup>29</sup> Thus, questions remain on the existence, extent, and origin of its interlayer interaction of the twisted graphene system.

We present a comprehensive picture of electronic dispersion in TBG, the simplest twisted graphene system, based on ARPES and density functional theory (DFT) calculations. We observed a band topology consisting of two non-interacting Dirac cones near  $E_D$ , and vHs and associated mini-gaps away from  $E_D$ , where the two layers’ Dirac cones overlap. Our experimental results provide unambiguous evidence of the interlayer interaction in TBG. What is more, we observed additional mini-gaps at the boundaries of the superlattice BZ associated with the moiré that evolves as two graphene lattices are rotated with respect to one another. Our results show that a moiré superlattice gives rise to a periodic potential, altering the electronic dispersion across the entire BZ according to its long-range periodicity and not just

where the states from two layers overlap. These observations illustrate how electronic dispersion is modulated by the moiré, a structure ubiquitous in superimposed two-dimensional (2D) lattices (e.g., hybrid multilayer structures<sup>5,6</sup>).

We fabricated TBG samples by transferring graphene monolayers grown on copper foils via chemical vapor deposition,<sup>30,2,3</sup> onto single-crystalline epitaxial graphene monolayers grown on a hydrogen-terminated SiC(0001) (Si-face),<sup>31,32</sup> following ref. 33. This fabrication procedure results in  $>100\mu\text{m}$  domains with random rotational orientation between two graphene lattices. Within each domain, the twist angle is relatively constant.<sup>34</sup> Such samples allow a systematic ARPES study of electronic dispersion primarily on a single domain with minimal effect from the underlying substrate.<sup>35</sup> The underlayer's Dirac cone is fixed in momentum space ( $k$ -space), while the overlayer's rotates about the  $\Gamma$ -point of the first primitive BZ, depending on the twist angle,  $\theta$ .<sup>33</sup> ARPES measurements were conducted at Beamline 7.0 of the Advanced Light Source,<sup>36</sup> using 95eV photons, a spot size of  $\sim 50 \times 100 \mu\text{m}^2$ , and sample  $T \sim 100\text{K}$ . Given the photon spot size, morphological variations at the micron-scale<sup>23</sup> are averaged out in the ARPES measurement. Overall energy resolution was  $\sim 60\text{meV}$ .

DFT calculations were conducted using VASP,<sup>37</sup> with the Ceperley-Alder Local Density Functional,<sup>38</sup> as parameterized by Perdew and Zunger,<sup>39</sup> in the Projector Augmented Wave Approximation.<sup>40</sup> DFT inherently describes any interlayer electron hopping, and interaction. We used a 400eV plane-wave basis cutoff. Correspondingly, optimization of single-layer graphene yielded a C-C separation of 1.41Å. Following Shallcross, *et al.*,<sup>15</sup> we constructed a table of commensurate-moiré cell sizes, which revealed that a  $11.64^\circ$  twist angle corresponds to a TBG supercell with a repeat distance of 8.54Å containing 292 carbon atoms (146 in each layer). This cell corresponds to Shallcross's parameters  $p=3$ ,  $q=17$ . The electronic band structure at this twist angle was computed for comparison to the ARPES data of nominally  $\theta \sim 11.6^\circ$ . We first obtained a self-consistent TBG charge density corresponding to a  $9 \times 9$  equally-spaced sample of the 2D superlattice BZ that included the zone center. We then computed energy levels using that density. With a bilayer separation of 3.4Å, LDA forces on carbon atoms along the bilayer normal were  $< 0.02\text{eV}/\text{Å}$ .

In the plots shown here, calculated DFT data are shifted to align  $E_D$  with the Fermi level ( $E_F$ ), expanded by 13% in energy to account for many-body interactions,<sup>41</sup> and adjusted for the average doping of the sample.<sup>42</sup> The doping level (50meV) was estimated so that the DFT data best match the ARPES data along two high symmetry directions (Figs. 2 (d) and (e)). Unequal carrier concentrations between two graphene sheets were not considered in the calculation.

The electronic states of TBG can be described by two primitive BZs having a twist angle between them. The case of  $\theta=11.64^\circ$  is illustrated in Fig. 1(a). The red hexagon is the primitive BZ for the underlayer graphene; the blue one corresponds to the overlayer graphene. The two small half circles overlaid on Figs. 1(a) and (b) are the measured photoemission intensity from two Dirac cones of TBG with  $\theta \sim 11.6^\circ$ .<sup>43</sup> These intensities are the constant energy contour at 0.4eV below  $E_F$ , which intersects the overlayer and underlayer cones centered at the  $K$ - and  $K_\theta$ -points, respectively.<sup>44</sup> Complete separation of the photoemission intensity evidences that there is no sign of interaction between the cones close to  $E_D$ .

The overlayer and underlayer cones exhibit slightly different spectra as seen in Fig. 1(c), which shows photoemission spectra along the line connecting  $K$ - and  $K_\theta$ -points. Owing to photoelectron attenuation, the underlayer cone (left cone at  $K$ -point) displays slightly lower intensity. Moreover, although the overlayer and the underlayer graphene sheets are both  $p$ -doped, their carrier concentrations appear slightly different as evidenced by their dispersions near  $E_D$ . That is, the size of the overlayer Fermi

surface (or the opening of the cone at  $E_F$ ) is slightly smaller than the underlayer's with  $E_D$  at about  $E_F+0.15\text{eV}$  and  $E_F+0.2\text{eV}$  for over- and underlayer, respectively. This small shift in  $E_D$  is attributable to the smaller influence of the substrate on the overlayer, a result of screening. Correspondingly, epitaxial graphene on hydrogen-terminated SiC is slightly p-type.<sup>32,45</sup>

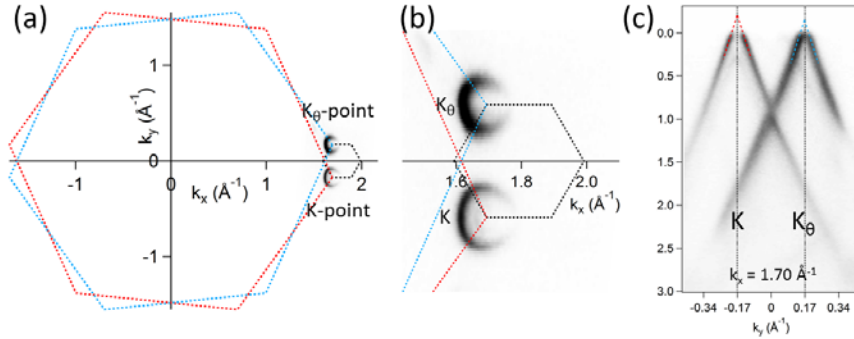


Figure 1  $k$ -space representation of TBG with  $\theta \sim 11.6^\circ$ . (a) Photoemission intensity contour of the two Dirac cones at the electron energy  $E_F - 0.4\text{eV}$ , and the primitive BZs of the underlayer and overlayer (red and blue hexagons). Darker shades indicate higher photoemission intensities. The small black hexagon is the moiré superlattice BZ of the  $(p,q)=(3,17)$  commensurate TBG. (b) Enlarged image of (a) near the two cones. (c) Photoemission spectra intersecting two cones at  $K$ - and  $K_\theta$ -points. The red and blue dash lines illustrate the under- and overlayer cones obtained by extrapolating the measured dispersions.<sup>46</sup>

Unlike near  $E_D$ , interactions between the two Dirac cones *are* observed at higher electron binding energy. Figs. 2(a-c) show photoemission intensity patterns at  $E_F - 0.8\text{eV}$ ,  $-1.0\text{eV}$ , and  $-1.3\text{eV}$ , where the contours of the cones deviate significantly from the expected circular-to-triangular band topology of monolayer graphene.<sup>47</sup> The superlattice BZ (black hexagon) and its high symmetry points,  $\Gamma_s$ ,  $K_s$ , and  $K'_s$  are overlaid on these experimental curves to highlight the superlattice's influence on the interlayer interaction. [n.b., throughout, subscript "s" indicates high-symmetry points associated with the *superlattice* BZ.] Note that while the cones exhibited "monolayer-like" topology near  $E_D$  (Figs. 1(a) and 2(a)), at higher binding energy, the two bands merge near  $K'_s$ -point (Fig. 2(b)). This is a first indication of their interaction. At this intersection, nested parallel bands emerge to the left of the cones (i.e., towards the origin in  $k$ -space as indicated by a red arrow, Figs. 2(b) and (c)), which exhibit an anti-crossing behavior. This same behavior is not seen towards the right (cf., the blue arrow in Fig. 2(b)). The reason is addressed below.

Emergence of the anti-crossing of the two bands, or *mini-gap* formation, results from coupling between the two Dirac cones. To illustrate, Fig. 2(d) displays the photoemission spectra along the horizontal black arrow in Fig. 2(c), which bisects the two cones. Note that the  $\pi$ -state is split around  $K'_s$ -point (cf., the red arrow). This splitting is also seen in the DFT electronic levels (blue dots in Fig. 2(d)). The anti-crossing behavior can be understood in terms of van Hove singularities (vHs), when the orthogonal direction (vertical black arrow in Fig. 2(c)) is examined. Fig. 2(e) shows photoemission spectra and DFT results along this direction, where the upper "M"-shape and the lower inverted "V"-shape bands correspond to the left and right nested parallel bands in Fig. 2(c). Noting that the "M"-shaped band in Fig. 2(e) is same as the upper split state in Fig. 2(d), it is apparent that these states have both positive and negative masses, creating a saddle point. Thus, as a consequence of coupling between the two layers' cones, vHs occur at the anti-crossing.

Besides the vHs, faint states reside within the mini-gap near the red arrows in Figs. 2(c) and (e); however, they do not appear in the DFT calculation. We postulate that they are due to the areas where the

interaction between two layers is reduced within a TBG domain. Such locations are attributable to topographical defects like ripples and blisters.<sup>48</sup> Low energy electron and atomic force micrographs support their presence on a length scale much smaller than our photon spot.

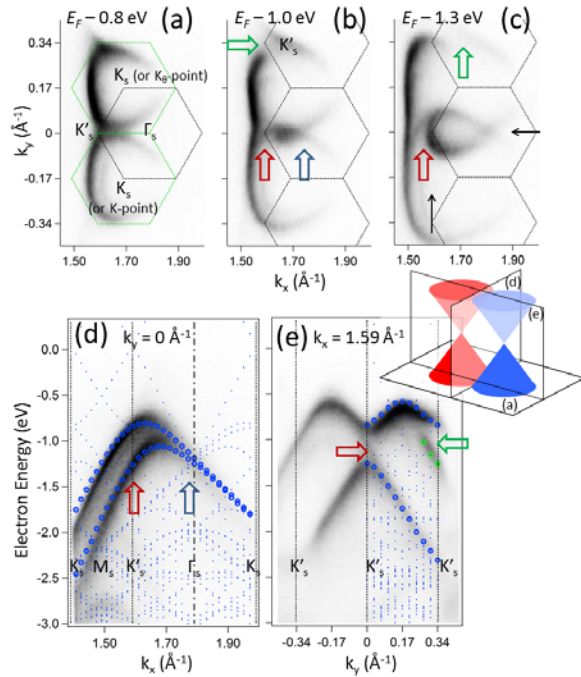


Figure 2 Electronic dispersions of the two interacting Dirac cones ( $\theta \approx 11.6^\circ$ ). (a-c) Photoemission intensity contours at  $E_F = 0.8 \text{ eV}$  (a),  $E_F = 1.0 \text{ eV}$  (b), and  $E_F = 1.3 \text{ eV}$  (c). Black hexagons indicate the moiré superlattice BZ of the commensurate TBG.  $\Gamma_s$ ,  $K_s$ , and  $K'_s$  are among its high symmetry points.  $K$ - and  $K_0$ -points are both  $K_s$ -points in the superlattice BZ. Green hexagons are minizones of a continuum model with a Dirac point at its zone center. (d) Photoemission spectra and the DFT states bisecting the two cones, and (e) the one orthogonal to (d). Their directions are indicated in (c) by horizontal and vertical black arrows. The schematic to the right of (e) shows the orientations of the photoemission patterns relative to the two primitive Dirac cones without interaction. DFT states are shown as blue dots. Calculated states matching the ARPES data are highlighted by blue and green circles.

The photoemission intensity contours shown in Fig. 2 include an additional interacting feature not explained by direct interaction of the two layers' Dirac cones. The green arrows in Figs. 2(b) and (c) highlight a splitting in the overlayer cone around  $K'_s$ -point, along a direction extending into the upper-left superlattice BZ. For more details, we take a second derivative of the photoemission intensity with respect to electron energy, as shown in Fig. 3. Red and blue circles in Fig. 3(a) highlight under- and overlayer cones, and help illustrate that the new feature appears not as a consequence of these cones' intersection, but because of the presence of a "new" cone centered on the moiré superlattice  $K'_s$ -point (black circle). Its dispersion is displayed in Fig. 3(b), along a line from this new (black) cone to the overlayer (blue) cone (i.e., the green arrow in Fig. 3(a)). Similar to the vHs observed in Fig. 2(e), an additional vHs is observed in both the ARPES and DFT results in Fig. 3(b). We attribute this new cone and the additional vHs forming along with it to adiabatic Umklapp scattering in the superlattice periodic potential.<sup>49,50</sup> They could not be present if the electrons of one layer were not responding to the periodic potential imposed by the other, thus, confirming that the two graphene layers are not isolated, but sense each other.

The ramifications of the periodic potential applied to graphene (in this case induced by a moiré superlattice) should have intriguing consequences.<sup>51,52,53</sup> In “normal” 2D materials, applying a periodic potential results in isotropic opening of the mini-gap over the entire boundary of the minizone defined by the potential’s periodicity. Graphene’s response is quite different because of the chiral (pseudo-spin) nature of the wave functions. Accordingly, the periodic potential does not open the mini-gap along the entirety of the minizone boundary but only at certain locations. Thus, moving along the minizone boundary, gaps will emerge and disappear.

To examine this effect, following Park *et al.*,<sup>52</sup> we define the minizone (green hexagons in Fig. 2(a)) by translating the superlattice BZ, so the center of the superlattice BZ matches K- and K<sub>θ</sub>-points. The line connecting K’<sub>s</sub>- and Γ<sub>s</sub>-points is along the minizone boundary.<sup>54</sup> In this view, coexistence of band splitting and crossing (shown by ARPES and DFT, red and blue arrows in Fig. 2(d)) is a consequence of the periodic potential induced by the moiré superlattice. Hence, the non-constant gap occurs because of graphene’s chiral wave functions.

Supporting this conclusion, the periodic potentials of a moiré should vary on a much longer length scale than the interatomic distance. Thus, a slight shift of one graphene sheet relative to another should only affect the electronic dispersion of TBG weakly. DFT calculations involving translations of one of the two graphene sheets by a fraction of interatomic distance confirm this. We conclude that TBG’s electronic dispersion evolves from two rotated graphene sheets subject to a long-range potential of the moiré superlattice evolving between them. Alternatively, TBG comprises two graphene sheets each subject to a periodic potential. This provides a simple way to understand many of the unique features alluded to in previous theoretical studies.<sup>52,53</sup>

Incidentally, the additional interacting state does not appear at the underlayer cone highlighted by the red circle in the data presented, but did appear in other data for different (typically smaller) twist angles.<sup>55</sup> If there is yet another “new” Dirac cone present in Fig. 3(a), we expect it to be centered on  $k_x \sim 1.4 \text{ \AA}^{-1}$ ,  $k_y \sim -0.34 \text{ \AA}^{-1}$ , and have the band topology similar to the “new” cone highlighted by the black circle. Although there is a state near where we expect to see the “new” cone, its shape is quite different. We therefore suspect that the data at the lower  $k_y$  in Fig. 3(a) originate from another TBG domain having a slightly different twist angle.

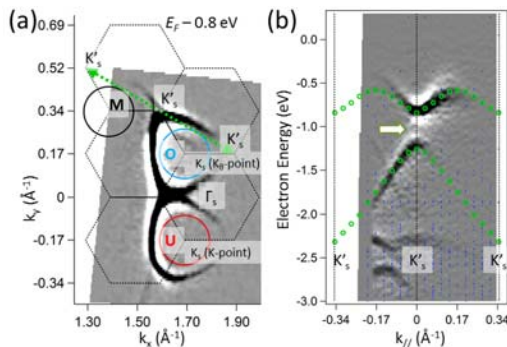


Figure 3 Second derivative of the ARPES intensity with respect to the energy ( $\theta \sim 11.6^\circ$ ). (a) Contours at  $E_F - 0.8 \text{ eV}$ . The black hexagons are the superlattice BZ. The Red, blue, and black circles with “U”, “O” and “M” illustrate the locations of underlayer-, overlayer, and moiré superlattice Dirac cones. (b) Processed photoemission pattern along the green arrow in (a) and DFT states (blue dots) connecting  $K'_s$ - $K'_s$ - $K'_s$  points. Green circles highlight DFT states matching the ARPES data.

Regions of AB stacking in the moiré superlattice dominate the interlayer interaction for twist angles  $>5^\circ$ ,<sup>18</sup> resulting in the mini-gaps seen in Fig. 4. Figs. 4(b) and (d) show the energy distribution curves (EDCs) halfway between the K- and  $K_\theta$ -points. For twist angles of  $\sim 5$  to  $\sim 12^\circ$ , the energy separation (peak-to-peak) stays near  $\sim 0.2\text{eV}$  (cf. the red arrows). This value is of the same order of magnitude as the interlayer interaction parameter of Bernal bilayer graphene,  $\sim 0.4\text{eV}$ .<sup>56</sup> We attribute the relatively unvarying magnitude of the mini-gap with twist angle to the persistence of local AB stacking within the moiré.<sup>57</sup> The large real-space moiré superlattice ensures the existence of AB stacking for all twist angles.

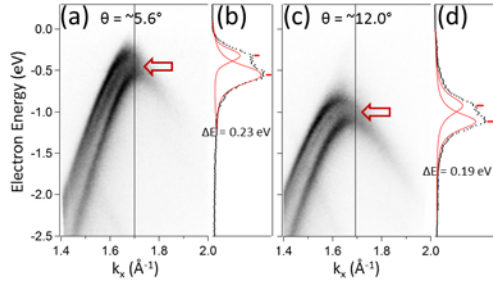


Figure 4 Photoemission intensity patterns (a,c) and EDCs (b,d) displaying the mini-gap as a function of  $\theta$ . (a,b)  $\theta \sim 5.6^\circ$ , (c,d)  $\theta \sim 12.0^\circ$ . Photoemission pattern bisects the two cones similarly to Fig. 2 (d). (b) and (d) are EDCs at the black lines in (a) and (c) fitted to Voigt functions (red lines).

Lastly, we offer plausible rationales for the absence of some of our DFT energy levels in the corresponding ARPES data (see small blue dots in Figs. 2(d,e) and 3(b)). First, the structure factor associated with ARPES may preferentially increase the intensity of certain states. This has been observed in measurements wherein intensities are strongly enhanced when a surface state overlaps a bulk state in  $k$ -space.<sup>58</sup> Following this argument, we presume that the TBG states overlapping those of a non-interacting graphene sheet would appear strongly in the ARPES measurement. Consequently, the measured photoemission intensity matches only a small subset of the DFT calculated states. Disorder in the TBG including mechanical distortions provides another possibility. As we saw via low energy electron diffraction, the twist angle in our samples varied slightly, over a few  $\mu\text{m}$  length-scale.<sup>33,34,59</sup> Because of the small superlattice BZ, the experimentally observed states from slightly different twist angles would be broadened with their intensity decaying rapidly, especially for those created by folding at superlattice BZ boundaries. The likelihood of observing these folded states would decrease correspondingly.

To close, coupling between the electronic states and the superlattice periodic potential have important implications for twisted multilayer graphene and hybrid 2D multilayer stacks. Based on our study of TBG, the superlattice BZ of a multilayer graphene ( $>$ three layers) is expected to be smaller (thus longer periodicity in real space). Previous theoretical work has shown that with an increase in spatial period, the apparent mini-gap shrinks,<sup>52</sup> leading to effectively non-interacting states. This is consistent with reported experimental results.<sup>27</sup> Second, any hybrid multilayers based on transferring 2D materials will unavoidably induce moiré superlattices and thus subject the system to a periodic potential. This potential influences the dispersion and thus the properties of the multilayer stack. Although transfer techniques now offer the possibility of a wider class of 2D materials<sup>60,61</sup> much as heteroepitaxial growth does,<sup>62</sup> understanding how these layers change as they are stacked together and mutually interact is prerequisite to leveraging their properties.

We are grateful to N. Bartelt, G. L. Kellogg, S. K. Lyo, and D. C. Tsui for fruitful discussions, and R. Guild Copeland and Anthony McDonald for sample preparation and characterization. J.T.R. is grateful for experimental assistance from F. Keith Perkins on sample growth. The work at SNL was supported by the US DOE Office of Basic Energy Sciences (BES), Division of Materials Science and Engineering and by Sandia LDRD. Sandia National Laboratories is a multi-program laboratory managed and operated by Sandia Corporation, a wholly owned subsidiary of Lockheed Martin Corporation, for the U.S. Department of Energy's National Nuclear Security Administration under contract DE-AC04-94AL85000. Work was performed at Advanced Light Source, LBNL, supported by the U.S. DOE, BES under Contract No. DE-AC02-05CH11231. The work at NRL was funded by the Office of Naval Research and NRL's NanoScience Institute.

- 
- <sup>1</sup> A. H. Castro Neto, *et al.*, Rev. Mod. Phys. 81, 109 (2009).
  - <sup>2</sup> X. Li, *et al.*, Science, 324, 1312 (2009).
  - <sup>3</sup> X. Li, *et al.*, Journal of the American Chemical Society, 133, 2816 (2011).
  - <sup>4</sup> M. Yankowitz, *et al.*, Nature Physics 8, 382 (2012).
  - <sup>5</sup> L. Britnell, *et al.*, Science 335, 947 (2012).
  - <sup>6</sup> H. Yan, *et al.*, Nature Nanotechnology, 7, 330 (2012).
  - <sup>7</sup> A. Reina, *et al.*, Nano Lett., 9, 30 (2009).
  - <sup>8</sup> J. Hass, *et al.*, Phys. Rev. Lett 100, 125504 (2008).
  - <sup>9</sup> S. Nie, *et al.*, Submitted.
  - <sup>10</sup> K. Kim, *et al.*, Nature 457, 706 (2009).
  - <sup>11</sup> S. Pang, Y. Hernandez, X. Feng, K. Müllen, Advanced Materials 23, 2779 (2011).
  - <sup>12</sup> S. Ghosh, *et al.*, Nature Materials 9, 555 (2010).
  - <sup>13</sup> A. H. MacDonald & R. Bistritzer, Nature 474, 453 (2011).
  - <sup>14</sup> J. M. B. Lopes dos Santos, N. M. R. Peres, and A. H. Castro Neto, Phys. Rev. Lett. 99, 256802 (2007).
  - <sup>15</sup> S. Shallcross, S. Sharma, and O. A. Pankratov, Phys. Rev. Lett. 101, 056803 (2008).
  - <sup>16</sup> G. Trambly De Laissardière, D. Mayou, L. Magaud, Nano Letters, 10, 804 (2010).
  - <sup>17</sup> E. J. Mele, Phys. Rev. B 84, 235439 (2011).
  - <sup>18</sup> R. Bistritzer and A. H. MacDonald, PNAS, 108, 12233 (2011).
  - <sup>19</sup> H. Schmidt, *et al.*, Appl. Phys. Lett. 93, 172108 (2008).
  - <sup>20</sup> J. D. Sanchez-Yamagishi, *et al.*, Phys. Rev. Lett. 108, 076601 (2012).
  - <sup>21</sup> G. Li, *et al.*, Nature Physics 6, 109 (2010).
  - <sup>22</sup> A. Luican, *et al.*, Phys. Rev. Lett. 106, 126802 (2011).
  - <sup>23</sup> K. Kim, *et al.*, Phys. Rev. Lett. 108, 246103 (2012).
  - <sup>24</sup> A. Righi, *et al.*, Phys. Rev. B 84, 241409(R) (2011).
  - <sup>25</sup> M. Sprinkle, *et al.*, Phys. Rev. Lett. 103, 226803 (2009).
  - <sup>26</sup> D. A. Siegel, *et al.*, PNAS 108, 11365 (2011).
  - <sup>27</sup> J. Hicks, *et al.*, Phys. Rev. B 83, 205403 (2011).
  - <sup>28</sup> D. L. Miller, *et al.*, Nature Physics, 6, 811 (2010).
  - <sup>29</sup> C. Mathieu, *et al.*, Phys. Rev B 83, 235436 (2011).
  - <sup>30</sup> Graphene monolayers grown on copper foils via chemical vapor deposition typically consist of domains of a few 100  $\mu\text{m}$  in size with random orientations.
  - <sup>31</sup> K. V. Emtsev, *et al.*, Nature Materials 8, 203 (2009).
  - <sup>32</sup> C. Riedl, *et al.*, Phys. Rev. Lett. 103, 246804 (2009).
  - <sup>33</sup> T. Ohta, T. E. Beechem, J. Robinson, G. L. Kellogg, Phys. Rev. B, 85, 075415 (2012).
  - <sup>34</sup> Using low energy electron microscopy and diffraction, we determined that the twist angle within each domain can vary up to  $1^\circ$ , and typically has  $\leq 0.5^\circ$  variation over a few to tens of  $\mu\text{m}$  length-scale.
  - <sup>35</sup> A. Bostwick, *et al.*, Science 328, 999 (2010).
  - <sup>36</sup> Scienta R4000 electron energy analyzer.

- 
- <sup>37</sup> G. Kresse and J. Furthmüller, *Comput. Mater. Sci.* 6, 15(1996); *Phys. Rev. B* 54, 11 169 (1996).
- <sup>38</sup> D. M. Ceperley and B. J. Alder, *Phys. Rev. Lett.* 45, 566(1980).
- <sup>39</sup> J. P. Perdew, A. Zunger, *Phys. Rev. B* 23, 5048(1981).
- <sup>40</sup> P. E. Blöchl, *Phys. Rev. B* 50, 17 953 (1994); G. Kresse and D. Joubert, *Phys. Rev. B* 59, 1758 (1999).
- <sup>41</sup> C. Heske, *et al.*, *Phys. Rev. B* 59, 4680 (1999).
- <sup>42</sup> T. Ohta, *et al.*, *Phys. Rev. Lett.* 98, 206802 (2007).
- <sup>43</sup> The twist angle is estimated from the ARPES data. The measured photoemission intensity is suppressed on one side of BZ due to interference effects between the two equivalent sublattices in graphene. E. L. Shirley, L. J. Terminello, A. Santoni, and F. J. Himpsel, *Phys. Rev. B* 51, 13 614 (1995).
- <sup>44</sup> The other cones located at the corners of primitive BZs ( $K^-$ ,  $K'^-$ ,  $K_{\theta^-}$ ,  $K'_{\theta^-}$ -points) are not shown due to the limited  $k$ -space of the measurement.
- <sup>45</sup> A. L. Walter, *et al.*, *Phys. Rev. B* 84, 085410 (2011).
- <sup>46</sup> A faint state around  $E_F - 0.3$  eV in the left Dirac cone at K-point (underlayer) reflects a small coverage of the second layer in epitaxial graphene.
- <sup>47</sup> A. Bostwick, *et al.*, *Nature Physics* 3, 36 (2007).
- <sup>48</sup> N. Levy, *et al.*, *Science*, 329, 544 (2010).
- <sup>49</sup> A Mugarza and J E Ortega, *J. Phys.: Condens. Matter* 15, S3281 (2003).
- <sup>50</sup> D. C. Tsui, *et al.*, *Phys. Rev. Lett.* 40, 1667 (1978).
- <sup>51</sup> N. Shima, H. Aoki, *Phys. Rev. Lett.* 71, 4389 (1993).
- <sup>52</sup> C.-H. Park, *et al.*, *Nature Physics* 4, 213 (2008).
- <sup>53</sup> M. Barbier, F. M. Peeters, P. Vasilopoulos, and J. Milton Pereira, Jr., *Phys. Rev. B* 77, 115446 (2008).
- <sup>54</sup> To avoid confusions, we use the word “minizone” used for continuum models, which typically define the bottom of a parabolic state (equivalent to the Dirac crossing point) as the zone center. The superlattice BZ has the reciprocal lattice vectors same to the ones of “minizone,” but the Dirac points are located at the corners.
- <sup>55</sup> Given the precision of the sample goniometer we used for ARPES, we can typically acquire data from an area of the sample amounting to  $\sim 50 \times 100 \mu\text{m}^2$  if the sample tilt is no more than  $\sim 5^\circ$ . Near the Dirac point in our measurement, this tilt angle range corresponds to  $\sim 0.4 \text{ \AA}^{-1}$  in reciprocal space.
- <sup>56</sup> T. Ohta, *et al.*, *Science* 313, 951 (2006).
- <sup>57</sup> G. Trambly de Laissardière, D. Mayou, L. Magaud, arXiv:1203.3144.
- <sup>58</sup> Ph. Hofmann, *et al.*, *Phys. Rev. B* 66, 245422 (2002).
- <sup>59</sup> T. E. Beechem, B. Diaconescu, T. Ohta, J. Robinson, unpublished.
- <sup>60</sup> B. Radisavljevic, M. B. Whitwick, and A. Kis, *ACS Nano*, 5, 9934 (2011).
- <sup>61</sup> D. Kim, *et al.*, *Nature Physics*, Published online (2012).
- <sup>62</sup> T. Ando, A. B. Fowler, and F. Stern, *Rev. Mod. Phys.* 54, 437–672 (1982), and the references therein.